Fractal Dimension of Irregular Region of Interest Application to Corn Phenology Characterization

Yonglin Shen, Xiuguo Liu, *Member, IEEE*, and Xiaohui Yuan, *Senior Member, IEEE*

***Abstract*—Analysis of multitemporal remote sensing imagery offers a reliable and cost-effective means for monitoring crops on a broad-scale and provides consistent temporal measurements. Fractal geometry has been used as a quantitative description of spatial complexity of remote sensing images. Yet, corn field of spatial irregularity alters the fractal dimension of the landscape, which shall be suppressed in the estimation. In this paper, we propose a method for computing fractal dimension from irregular region of interests that minimizes the contribution from 2-D spatial irregularity. Our method was evaluated with normalized difference vegetation index products derived from moderate resolution imaging spectroradiometer and satellite pour l'observation de la terre VEGETATION sensors from three states in the U.S. The experimental results using the time series demonstrated that our proposed fractal dimension estimation method exhibited great consistency and invariance to the change of image spectral characteristics, spatial resolution, and the degree of pixel mixing. In contrast to entropy and variance, the spectral characteristics of different imaging devices exhibited lower impact to the fractal dimension, which also implies its scale invariance. With respect to the detection rate of the first peak, fractal dimension achieved the best consistency. The proposed method for computing fractal dimension provides a critical and reliable measure for studying phenological patterns.**

***Index Terms*—Fractal dimension, normalized difference vegetation index (NDVI), texture.**

I. Introduction

PHENOLOGY varies over the life cycle of crops [1], which leads to diverse phenological patterns in timing, frequency, duration, and degree of synchrony [2]. Analysis of multitemporal remote sensing imagery offers a reliable and cost-effective means for monitoring crops on a broad scale and provides consistent temporal measurements [3]. Detecting the dynamics of phenology activities is a prerequisite toward phenology-related applications [4], and characterizing crop phenology is the key.

Manuscript received August 14, 2016; revised November 22, 2016; accepted December 17, 2016. This work was supported in part by the National Natural Science Foundation of China under Grant 41501459. *(Corresponding author: Xiaohui Yuan).*

Y. Shen and X. Liu are with the Faculty of Information Engineering, China University of Geosciences, Wuhan 430074, China (e-mail: yonglinshen@gmail.com; liuxg318@163.com).

X. Yuan is with the Faculty of Information Engineering, China University of Geosciences, Wuhan 430074, China, and also with the Department of Computer Science and Engineering, University of North Texas, Denton, TX 76203 USA (e-mail: xiaohui.yuan@unt.edu).

Color versions of one or more of the figures in this paper are available online at http://ieeexplore.ieee.org.

Digital Object Identifier 10.1109/JSTARS.2016.2645880

Normalized difference vegetation index (NDVI) provides a perspective of biotic activities [5] and has been widely employed in phenology-related research [6], [7]. Conventional phenology detection approaches using multitemporal satellite data mainly take spectral responses into account [8], [9]. However, NDVI-based phenology studies are confronted by the problems of spectral characteristics, spatial resolution, temporal coverage, mixed pixels, etc., which affect the consistency of phenology characterization. To quantitatively characterize phenology dynamics, descriptive features from NDVI data that are scale invariant and robust to irregular spatial region need to be studied.

Fractals are patterns that are self-similar across different scales. Fractal dimension [10] provides a metric to evaluate the complexity of the repeating structures in fractal patterns. In contrast to the conventional feature descriptors such as color histogram, cooccurrence matrix, and entropy, fractal dimension gives a quantitative evaluation that is independent from the scale, which makes it a highly promising metric for the evaluation of remote sensing imagery that varies in resolution. Corn fields at different progress stages contribute to the variation in NDVI [8]. Soil background effects and density of corn leaf canopy affect the roughness of an NDVI image. Each such image corresponds to a data point in the fractal dimension time series, which follows a bimodal distribution throughout the life cycle of corn crops. The two peaks in the time series correspond to the emerged and harvested stages [11]. The variation of the spatial pattern in an NDVI image provides a critical and reliable perspective for analyzing the growth of crops.

Research has been conducted to apply fractals to various real-world problems, e.g., image classification [12], spatial scaling correction [13], urban landscapes [14], and forested landscapes [15]. Fractal analysis has been applied to multiresolution remote sensing images for landscape characterization [16]–[19]. Amri *et al.* [20] used fractals to quantitatively characterize NDVI dynamics. Liang *et al.* [14] evaluated the effectiveness of diverse fractal algorithms in the characterization of urban landscapes based on satellite images taken by diverse sensors. Al-Hamdan *et al.* [15] investigated the applications of fractal measurements to different spatial, temporal, and spectral resolutions of remote sensing data acquired from different sensors. However, in aspect of corn phenology characterization, corn fields are usually depicted in an irregular region of interest (ROI) in an image, whereas fractal dimension estimations are often performed with regular ROIs, e.g., a square region in an image. The fractal dimension encapsulates the irregularity in a 3-D space. Yet, components from spatial irregularity alter the fractal dimension of

the landscape and shall be suppressed in the estimation. Hence, the scalability of fractals in irregular ROIs requires further investigation.

There exist indirect strategies for estimating the fractal dimension of irregular ROIs, e.g., partially cutting method [21], which segments a regular sample from the whole ROI, then estimates the fractal dimension following the conventional fractal dimension estimation procedure. The mean local fractal dimension method [22] estimates each pixel in the whole ROI with a local fractal dimension estimation algorithm, then calculates the mean fractal dimension of the ROI. However, the accuracy of these strategies will be affected by the nonuniform distribution of corn pixels in the remote sensing imagery, even makes the estimation inestimably. In addition, Klinkenberg [23] tried using the dimensionality reduction technique to estimate the fractal dimension of 3-D surface. The basic principle is that higher dimensional spaces can be built up systematically as direct products of fractals in lower dimensional spaces. While in Klinkenberg's approach, the fractal dimension of surface was estimated only by calculating the fractal dimension of contours extracted from the surface, and then, increasing by 1 to account for the difference. The limitation is that the fractal dimension of the contours or profiles in a certain position of surface equals not to other positions for a nature surface.

Image resolution and scale greatly affect the appearance of ground objects in remote-sensed imagery. Conventional texture metrics require a scale to compute the feature descriptor, e.g., entropy, which makes the application of these methods highly sensitive to the choice of the scale parameter, which is usually determined empirically. We hypothesize that by circumventing the spatial and scale constraints, fractal dimension serves as a highly competitive feature descriptor for describing complex ground patterns, and hence, is appropriate for phenology analysis. In this paper, we propose a method for computing the fractal dimension of regions with irregular ROIs to minimize the contribution from spatial irregularity. We conduct a thorough evaluation of its efficacy and robustness to characterize corn phenology from NDVI time series. Pixels of corn field across different levels of pixel mixing follow a similar spatial distribution. Two criteria including similarity metric of time series and consistency metric of the key phenology stage are employed in our evaluation.

The rest of this paper is organized as follows: Section II presents phenology analysis using remote sensing methods and describes our methods for cropland masking using spatial inconsistent imagery data and fractal dimension metric for irregular ROIs. Section III presents our experimental data and evaluation criteria, and discusses the results. Section V concludes this paper with a summary.

II. Fractal-Based Corn Phenology Characterization

Fig. 1 illustrates the overall procedure of our phenology analysis. In our method, the time series of remote sensing images provides the temporal changes of the fields and each image is processed individually. With assistant of cropland mask, corn fields are delineated from each NDVI image. The scale

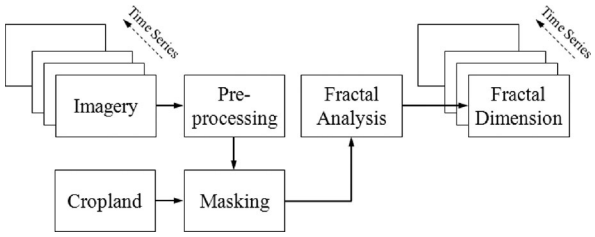

Fig. 1. Corn phenology analysis using NDVI data.

difference between NDVI image and the corn field mask is minimized in the preprocessing step. Yet, the masking process must address pixel mixing issue. The fractal analysis computes the fractal dimension of the corn fields by minimizing the impact from irregular ROIs.

A. Cropland Masking

Cropland masking employs an image mask to exclude the undesired noncorn regions in the image. Due to the inconsistency in the resolution of the mask and the image as well as the misalignment between them that induces a mixture of different land covers, a purity ratio is devised to measure the dominance of the corn components, and hence, decide if a pixel is considered a corn pixel and shall be included in fractal dimension calculation.

The image mask used in cropland masking is created either via a segmentation process or using an existing data product such as cropland data layer (CDL) [24] that is produced annually by the National Agricultural Statistics Service (NASS) of the United States Department of Agriculture (USDA). However, the spatial resolution of such a data product differs from year to year. For CDL data between 2006 and 2009, the spatial resolution is of 56 m, and that of the other years is 30 m. In addition, the scale difference to the NDVI imagery and misalignment also poses issues. We use a purity ratio to map an NDVI image to corn field segments for fractal analysis.

The purity ratio (denoted by ρ) for each NDVI pixel $N(a, b)$ is calculated with respect to the geo-registered cropland mask

$$\rho(a,b) = \frac{C(a,b)}{|N(a,b)|} \tag{1}$$

where $C(a, b)$ is the size of corn field in an NDVI pixel $N(a, b)$, and $|N(a, b)|$ denotes the spatial coverage of this NDVI pixel (e.g., $|N(a, b)|$ is 1 km^2 for a satellite pour l'observation de la terre VEGETATION (SPOT-VGT) image). The cropland size of an NDVI pixel is less than or equal to the NDVI pixel size, i.e., $C(a, b) \leq |N(a, b)|$. In a cropland mask M, pixels of crops and noncrops are represented with ones and zeros, respectively. Fig. 2 illustrates the georelation of cropland mask and the NDVI image. The top layer depicts an NDVI image and the bottom layer shows the cropland mask and the projected georegistered NDVI image, which is outlined with dash line. Due to the misalignment between two datasets, partial overlapping occurs as shown in Fig. 2, i.e., part of a cropland mask pixel is within an NDVI pixel by an offset of $\Delta x \geq 0$ and $\Delta y \geq 0$. Hence,

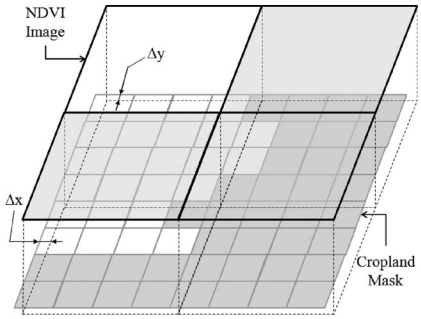

Fig. 2. Cropland masking and geoalignment. The top layer depicts an NDVI image and the bottom layer shows the cropland mask and the projected georegistered NDVI image (in dash line).

TABLE I
THRESHOLDS FOR DIFFERENTIATING NDVI PIXELS

Thresholds	NDVI Pixel Category	Image Modality
≈0%	corn-presence pixels	MODIS, SPOT-VGT
50%	partial pixel mixing	MODIS, SPOT-VGT
≈100%	corn-dominated pixels	MODIS

$C(a,b)$ can be computed as a summation of the size of the partially overlapped cropland mask pixels as follows:

$$C(a,b) = \sum_{a+\Delta x}^{a+\Delta x+|a|} \sum_{b+\Delta y}^{b+\Delta y+|b|} M(x,y) \tag{2}$$

where $|\cdot|$ gives the spatial size of a pixel in the respective dimension. When applying the purity ratio, a threshold is used to decide if an NDVI pixel is considered as a corn pixel. Assuming the threshold is 50%, the example depicted in Fig. 2 consists of three corn field pixels and one noncorn field pixel in the NDVI image. In general, increasing the threshold allows less amount of noncorn components in a NDVI pixel.

To understand the effect of using different purity ratios to the fractal dimension computation, our evaluation used three thresholds as listed in Table I. Partial pixel mixing and two extreme cases (corn-dominated pixel and corn-presence pixel) are considered. When the corn crop occupies an entire NDVI pixel (i.e., corn-dominated pixel), the NDVI of this pixel reflects the spectrum of corn. In case of partial pixel mixing, the majority of an NDVI pixel represents the spectrum reflection of corn. When corn weakly appears in the NDVI pixel (i.e., corn-presence pixel), an NDVI pixel allows contribution from the bare ground and other vegetation.

Three thresholds were set for the moderate resolution imaging spectroradiometer (MODIS) NDVI image, i.e., corn-presence pixel ($\rho \approx 0\%$), partial pixel mixing ($\rho = 50\%$), and corn-dominated pixel ($\rho \approx 100\%$); and partial pixel-mixing and corn-presence pixels were set for SPOT-VGT. Because only a few corn pixels remain in the masked image, the threshold of corn-dominated pixels was not used in the process of SPOT-VGT imagery [an example is shown in Fig. 5(f)].

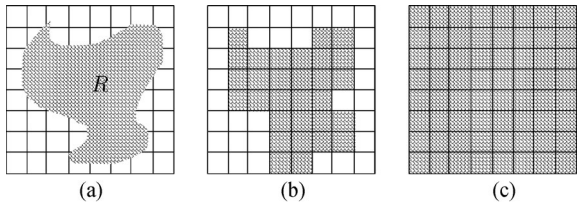

Fig. 3. Fractal dimension for characterizing cropland (depicted in gray shade) texture. (a) Cropland in a remote sensing image. (b) Masked cropland for fractal dimension. (c) Ideal ROI for fractal dimension calculation.

B. Fractal Dimension of Irregular ROI

Fractals offer advantages for texture analysis with minimum influence of scale due to their self-similarity property. Box-counting dimension is an intuitive way of computing fractal dimension. Given a manifold R in a metric space, the space is gridded into even cells (or boxes) of side length ϵ. $B(\epsilon; R)$ is the number of boxes to cover the manifold. The box-counting dimension $D(R)$ is the number of boxes as the side length of the boxes approaches zero

$$D(R) = \lim_{\epsilon \to 0} \frac{\log B(\epsilon; R)}{\log \frac{1}{\epsilon}} \tag{3}$$

where $B(\epsilon; R)$ is the number of boxes to fill the manifold R with a side length (or scale) ϵ. That is, by reducing the size of the boxes, we accurately capture the structure of the manifold. The fractal dimension allows us to characterize patterns and shapes quantitatively and is robust to the variance of object scale, which is common in real-world applications. Yet, remote sensing images are not strictly self-similar at all scales [25]; they may be at most only statistically self-similar over a limited range of scales [26]. The fractal dimension can maintain self-similarity over a large range of scales, and the scales used to estimate the fractal dimension in this study have been tested to fall within this range.

Croplands usually appear irregularly in remote sensing imagery as shown in Fig. 3(a). Of the wide variety of methods available for estimating fractal dimension, the computation is performed based on regular ROIs (mostly square regions) [26], [27]. Consider an NDVI image in a 3-D Euclidean space and the pixel value serves as the third dimension in this space. Hence, the image intensity is perceived as a rugged manifold. To address the spatial irregularity of the targeted regions in remote sensing data, the dimensionality reduction based differential box-counting (DR-DBC) method [11] was developed that integrates fractals in subspaces. The idea is based on the property that box-counting dimension is equivalent to the summation of the lower fractal dimensions of the subspaces [28]

$$\mathcal{D}(S \times S') = \mathcal{D}(S) + \mathcal{D}(S')$$

where $S \subseteq \Re^m$ and $S' \subseteq \Re^n$ and $\mathcal{D}(\cdot)$ denotes the box-counting dimension of a manifold spanning a space $R \times R'$. Hence, the fractal dimension of an irregular manifold R is the summation of the fractal dimensions of its subspaces

$$\mathcal{D}(R) = \mathcal{D}_z(R) + \mathcal{D}_{\mathrm{xy}}(R) \tag{4}$$

where $\mathcal{D}_z(R)$ is the fractal dimension of R in the vertical direction and $\mathcal{D}_{\mathrm{xy}}(R)$ is the fractal dimension of R in the horizontal plane $x-y$. This computation of fractal dimension also characterizes the spatial layout of the manifold as shown in Fig. 3(b), which induces error along the boundary of the target region because a cell may contain a mixture of croplands and noncroplands.

To compute the fractal dimension of R in 3-D space, the space is partitioned with cubes of scale ϵ in all dimensions, namely ϵ-cube. The box dimension of manifold R is computed following (3) [29]. The calculation of $B(\epsilon; R)$ requires dividing the space with ϵ-cube, and hence, we have

$$B(\epsilon; R) = \sum_{\epsilon^2 \in R} \left\lceil \frac{N^* - N_*}{\epsilon} \right\rceil \tag{5}$$

where N^* and N_* denote the maximum and minimum values of the NDVI pixels in a cube. $\epsilon^2 \in R$ denotes the cube lands in the cropland region of the NDVI image. In practice, the noncropland results in zero count of ϵ-boxes.

Note that the image size and the image color depth are not necessarily of the same scale. The ϵ-cube could be uneven on its sides. For instance, we can have a cube of $\epsilon \times \epsilon \times \epsilon'$, where $\epsilon \neq \epsilon'$. However, the algorithm for calculating the fractal dimension remains unchanged. For simplicity, we use ϵ-cube of equal sides in the rest of our discussion.

To compute $D_{\mathrm{xy}}(R)$ in (4), ϵ-box is used to fill the manifold R in $x-y$ plane. The algorithm follows the same idea as the one used for computing $D(R)$. Hence, the fractal dimension of R in the vertical direction, i.e., $D_z(R)$, is the difference of $D(R)$ and $D_{\mathrm{xy}}(R)$.

However, to characterize the texture of croplands, each cell (i.e., an NDVI pixel) contains only the measurements of crops in the ideal case. That is, the texture feature of the cropland is independent from the shape of the field. Hence, the computation of fractal dimension shall not account for the irregularity of the region of study.

Let $\mathcal{D}_\perp$ denote the fractal dimension of the manifold (i.e., the croplands in an NDVI image) that spans the entire field of view as shown in Fig. 3(c). $\mathcal{D}_\perp$ is, hence, proportional to $D(R)$ with an addition that fills the voids in the non-cropland areas [i.e., the cells without texture in Fig. 3(b)]. Such addition can be approximated with the difference between two dimension and the fractal dimension of manifold R in $x-y$ plane

$$\mathcal{D}_\perp(R) \propto \mathcal{D}(R) + (d - \mathcal{D}_{\mathrm{xy}}(R)) \tag{6}$$

where d is the full dimension of the subspace $x-y$.

$\mathcal{D}_\perp$ inherits the scale invariant property of box-counting dimension. Furthermore, it enables computing the fractal dimension of objects with irregular spatial region in images, and allows to characterize the phenology changes of corn crop.

III. Experimental Study

A. Datasets

Corn is the most widely grown grain crop in the United States. NDVI data have been acquired in three primary corn-producing districts in the U.S. Corn Belt, namely the states of Iowa (IA), Illinois (IL), and Nebraska (NE). The geographical locations are shown in Fig. 4. The three states occupy approximately 39.7% of the total U.S. corn harvested area in 2013. In our experiments, two types of NDVI products are derived from MODIS and SPOT-VGT [30], [31] sensors. These two datasets present a tradeoff between spatial and temporal resolutions [32]–[34]. The two products are briefly described as follows:

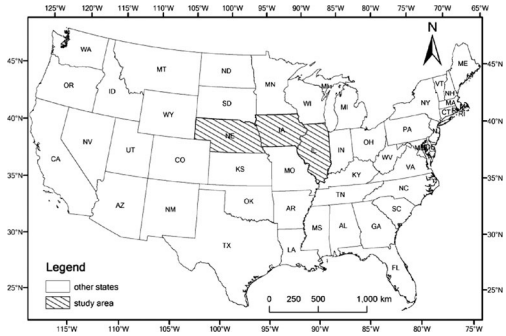

Fig. 4. Three states on the U.S. Corn Belt: Iowa, Illinois and Nebraska, where test data are collected from.

1) ***MODIS NDVI Time Series*** is derived from the atmospherically corrected MODIS MOD09GQ (MODIS Surface Reflectance Daily L2G Global 250 m) products at a spatial resolution of 250 m. The dataset is publicly available and distributed through the Vegetation Condition Explorer [35]. The daily MODIS NDVI was subsequently combined into the 10-day MODIS NDVI via the maximum-value composite (MVC) method [36]. The operation is considered with respect to two objectives, i.e., first, to minimize the effects of clouds and atmospheric constituents [37], and second, to maintain consistency with the SPOT-VGT dataset in terms of the temporal resolution. The periods of the compositing process are defined according to the calendar dates, i.e., from the 1st to the 10th, from the 11th to the 20th, and from the 21st to the end of each month.

2) ***SPOT-VGT NDVI Time Series*** is extracted from the SPOT-VGT S10 products at a spatial resolution of 1 km [38]. The S10 represents a 10-day global synthesis composited via the MVC method. The raw S10 products are provided in "Plate Carree projection," covering all of Central America. Postprocessing includes reprojection into the "USA Contiguous Albers Equal Area Conic projection (USGS version)" [24], and geographically clipped into regional subsets [39]. Each year from 2002 to 2011, 36 S10 datasets are acquired for this study from January 1 to December 21.

Fig. 5 illustrates examples of NDVI images derived from MODIS imagery and SPOT-VGT imagery. As we increase the thresholds for corn proportion, the available pixels (i.e., the pixels in gray) for calculating fractal dimension of corn fields decrease significantly. An extreme case is shown in Fig. 5(c), in which very few pixels remain for the fractal dimension computation.

B. Evaluation Criteria

In our analysis, a similarity metric for time series and a stability measure on the key phenology under diverse data acquisition

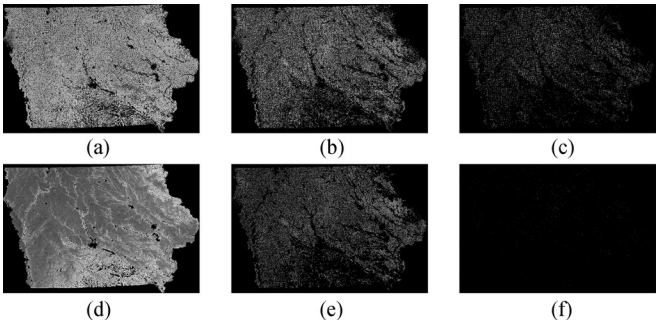

Fig. 5. NDVI images derived from MODIS and SPOT-VGT using three thresholds. (a) MODIS NDVI ($\rho \approx 0\%$). (b) MODIS NDVI ($\rho = 50\%$). (c) MODIS NDVI ($\rho \approx 100\%$). (d) SPOT-VGT NDVI ($\rho \approx 0\%$). (e) SPOT-VGT NDVI ($\rho = 50\%$). (f) SPOT-VGT NDVI ($\rho \approx 100\%$).

conditions were employed to evaluate the performance of our method. The rest of this section gives details on these metrics.

1) Similarity Metric for Time Series: A metric that measures the time-series similarities is critical to the evaluation of fractal dimension. In this study, we used cosine similarity [40] to measure the similarity of time series derived from diverse data acquisition conditions (e.g., difference in sensor, spatial resolution, and level of pixel mixing). The cosine similarity (a.k.a. spectral angle mapper [41]) has been widely used in hyperspectral remote sensing to measure spectral similarity of hyperspectral data, which is computed as follows:

$$\Theta(x, y) = \arccos\left(\frac{\langle x, y\rangle}{\|x\| \, \|y\|}\right) \frac{180}{\pi} \tag{7}$$

where $\langle\cdot\rangle$ denotes the inner product and $\|\cdot\|$ computes the norm of the vector. Because x and y are positive, $\Theta(x, y)$ is in $[0, 90^\circ]$. $\Theta(x, y)$ is proportional to the angle between two vectors x and y, i.e., the time series. The closer the cosine is to zero, the more similar the series are.

2) Stability Metric: The time series of fractal dimension is bimodal in the life cycle of corn crop. The first peak indicates the emerged stage of corn and the second peak indicates the harvested stage [11]. At the emerged stage, the corn leaf canopy shows increasing density. The soil background (depicted low NDVI value) and green corn leaves (depicted high NDVI value) are mixed together, which increase the roughness of the NDVI image. A similar situation occurs during the corn harvest period when corns are usually gathered from the field in days or longer. The roughness of NDVI image texture increases because certain fields are harvested and the others are not. The mixture of bare soil and the remaining leaves and stalks also increase the roughness of the NDVI image [11]. In this study, the harvested stage was not considered in the stability measurement, mainly because it belongs to the developmental stage and is more susceptible to interference by unconventional farming practices.

To detect the first peak in the annual time series, Timesat [42] was used in our study. The tool was designed to process time series data, in which an asymmetric double-Gaussian distribution [43] was used to portray the seasonal growth and decline curves of the corn crop, and to estimate the phenological parameters. Parameters were preliminarily set as a bimodal distribution together with approximate timing of the growing seasons. Timesat can reduce biased noise (in the MVC processed data), due to interference of clouds and atmospheric constituents. The asymmetric double-Gaussian distribution $g(t)$ is given by

$$g(t) = \begin{cases} \exp\left(-\left(\frac{t-a}{b_1}\right)^{c_1}\right), & \text{for } t > a \\ \exp\left(-\left(\frac{a-t}{b_2}\right)^{c_2}\right), & \text{otherwise} \end{cases} \tag{8}$$

where a determines the position of the maximum or minimum with respect to the independent time variable t, b_1 and b_2 determine the width of the function for the right half and left half, respectively, and c_1 and c_2 determine the kurtosis of the distribution. The details of the algorithm can be found in [43].

The stability of time series was assessed with the erroneous detection of the emerged stage and the frequency of missed peaks in the time series. The relative and absolute errors are evaluated following the root mean square error (RMSE) as follows:

$$\text{RMSE} = \sqrt{\frac{\sum_{t,i,j}\left(\hat{d}_{t,i,j} - \tilde{d}_{i,t}\right)^2}{n}} \tag{9}$$

where $\hat{d}$ is the detected day of the emerged stage, n is the total number of cases, and $\tilde{d}$ denotes the reference day. For the *absolute RMSE*, $\tilde{d}$ is the ground truth of the emerged stage; for the *relative RMSE*, $\tilde{d}$ is the average day of the predictions using different input data and features. To compute RMSE, we aggregate all cases of the study sites (denoted with i), cropland masking result (denoted with j), and years (denoted with t).

There are cases when the first peak was missed, which happens particularly when the number of corn pixels is small and there are strong noise. Hence, we used the number of failed detection as a metric to evaluate the robustness of fractal dimension on characterizing corn phenology.

C. Texture Features

In addition to the fractal dimension, we include widely used texture measures in our evaluation. The most commonly used measures of statistics-based texture descriptors include first-order (occurrence) statistics and second-order (cooccurrence) statistics [44], [45]. The first-order statistics measures assess the spectral properties of individual pixel values without account for the spatial relations among image pixels; whereas the second-order statistics take the spatial distribution of spectral values into account.

Texture measures of variance and entropy derived from remote sensing images have been used to characterize phenological variation [44]. The time series of variance and entropy represents a bimodal distribution throughout the corn life cycle, which is similar to the fractal dimension time series. Although the fractal dimension, variance and entropy can be used to indicate the heterogeneity of image texture, they place particular emphasis on different aspects. The variance measures the dispersion of an image or ROI around the mean intensity value, and entropy is a measure of disorder or complexity. Both variance

and entropy can be further calculated with first- and second-order statistics.

First-order statistics are derived from the histogram of an image or ROI. The first-order variance (denoted by $V_{1\text{st}}$) describes the deviation of intensity from the mean. The first-order entropy (denoted by $E_{1\text{st}}$) is a measure of histogram homogeneity. $V_{1\text{st}}$ and $E_{1\text{st}}$ are computed as follows:

$$V_{1\text{st}} = \frac{1}{N-1}\sum_{i=1}^{N}(x_i-\mu)^2 \tag{10}$$

$$E_{1\text{st}} = -\sum_{g=1}^{G} P(g)\log P(g) \tag{11}$$

where $\mu = \frac{1}{N}\sum_{j=1}^{N} x_j$; N and G are the number of pixels and distinct gray levels in the entire image or ROI, respectively; x_j is the gray value of pixel j; and $P(g)$ is the probability of occurrence of gray-level g.

Second-order statistics are derived from the gray-level cooccurrence matrix (GLCM). The GLCM is a symmetric $G \times G$ matrix, where G is the gray level. The matrix acts as an accumulator such that $P(i,j)$ is the number of occurrences of the pair of gray levels i and j. Pixel pairs are defined by a displacement vector $d = (\Delta x, \Delta y)$ covering the orientation and offset. Four typical displacement vectors with one neighboring pixel are $(0,1)$, $(-1,1)$, $(-1,0)$, and $(-1,-1)$. These vectors correspond to orientations of 0° (horizontal), 45° (right diagonal), 90° (vertical), and 135° (left diagonal), respectively. Mathematically, a normalized occurrence matrix P over an n by m image I is given by

$$P_d(i,j) = \frac{1}{N}\sum_{p=1}^{m}\sum_{q=1}^{n}\delta(p,q), \quad \text{and} \tag{12}$$

$$\delta(p,q) = \begin{cases} 1, & \text{for } I(p,q) = i \text{ and } I(p+\Delta x, q+\Delta y) = j \\ 0, & \text{otherwise} \end{cases}$$

where (p,q) is the pixel coordinate in the image; θ is the angle of neighboring pixels, i.e., $\theta = 0^\circ$, 45°, 90°, and 135°; and N is the total count of cooccurred gray-level pairs, i.e., $N = \sum_i \sum_j P_d(i,j)$. The second-order variance $V_{2\text{nd}}$ and entropy $E_{2\text{nd}}$ can be formulated based on the GLCM as follows:

$$V_{2\text{nd}} = \sum_i \sum_j \frac{(i-\mu_x)^2 + (j-\mu_y)^2}{2} P_d(i,j) \tag{13}$$

$$E_{2\text{nd}} = -\sum_i \sum_j P_d(i,j)\ \log P_d(i,j) \tag{14}$$

where $\mu_x = \sum_i iP(i,j)$ and $\mu_y = \sum_j jP(i,j)$. Complex textures tend to have high entropy. If the frequencies of occurrence in the cooccurrence matrix are equally scattered over the matrix, high values of entropy can be expected. This uniform scattering occurs when the largest spread of different pixel intensity occurs in the spectral image.

IV. Results and Discussion

A. A Phenology View From the Time Series of Features

In this study, a total of 11 features extracted from remote sensing images were employed to characterize corn phenology, which include fractal dimension (FD), first-order variance ($V_{1\text{st}}$), and entropy ($E_{1\text{st}}$), and second-order variance ($V^0_{2\text{nd}}$, $V^{45}_{2\text{nd}}$, $V^{90}_{2\text{nd}}$ and $V^{135}_{2\text{nd}}$) and entropy ($E^0_{2\text{nd}}$, $E^{45}_{2\text{nd}}$, $E^{90}_{2\text{nd}}$ and $E^{135}_{2\text{nd}}$) in four directions. The corresponding time series of the 11 features of Iowa state in 2011 are illustrated in Fig. 6. Each panel contains results from five cropland masked images. Using different degree of pixel mixing in cropland masking (i.e., the thresholds in Table I), following five cases can be derived from the MODIS and SPOT-VGI data:

1) M_g: MODIS data and corn-presence;
2) M_p: MODIS data and partial mixing;
3) M_c: MODIS data and corn dominated;
4) S_g: SPOT data and corn presence;
5) S_p: SPOT data and partial mixing.

Fig. 6 illustrates the time series of features using different cropland masked NDVI data. The time series exhibits a bimodal distribution. The first peak represents the emerged stage of corn crop, and the second peak represents the harvested stage. Fig. 6(d)–(g) depicts time series of four directional features. Comparing across the panels, e.g., M_p in all eight panels, it is evident that the time series of various directional features are very close. This implies that the texture of corn fields in the SPOT-VGT and MODIS images is mostly isotropic.

A range of abrupt low values exists in all curves of the features from different cropland masked images in Fig. 6, especially in the period from January 11 to February 11. Such low values are possibly caused by the snow coverage. When the ground is completely covered by snow, the spectral reflectance is mostly uniform. Therefore, the heterogeneity of corn fields in the remote sensing image is relatively low.

As shown in Fig. 6(b), the first-order variance of S_g changed near the two peaks. The roughness was more distinct than the variance with S_p, M_g, M_p, and M_c. In these two time periods, the crop change was due to the emergence of green corn leaf or harvesting. The mixture of soil background (with lower NDVI value) and green corn (with higher NDVI value) increased the roughness of the image texture. This trend also appears in the second-order variance, shown in Fig. 6(d)–(g). The mixture of soil background and corn leaves resulted in two significant peaks in the variance time series, and the impacts from the common effects of various sensors, spatial resolution and mixed pixels yielded great differences in these two stages.

As shown in Fig. 6(c), the first-order entropy of S_g was greater than that of M_g as a whole, mainly because the distribution of GLCM of S_g was more uniform than that of M_g. This figure also shows that the SPOT-VGT imagery of corn crop contains more noise than that of the MODIS sensor under the condition of corn-presence pixel. However, if only the neighbor pixels were considered, the second-order entropy were lower than the first-order entropy as a whole [see Fig. 6(h)–(k)]. The planting dates of corn crop were inconsistent across different fields over an entire state, which resulted in greater first-order entropy.

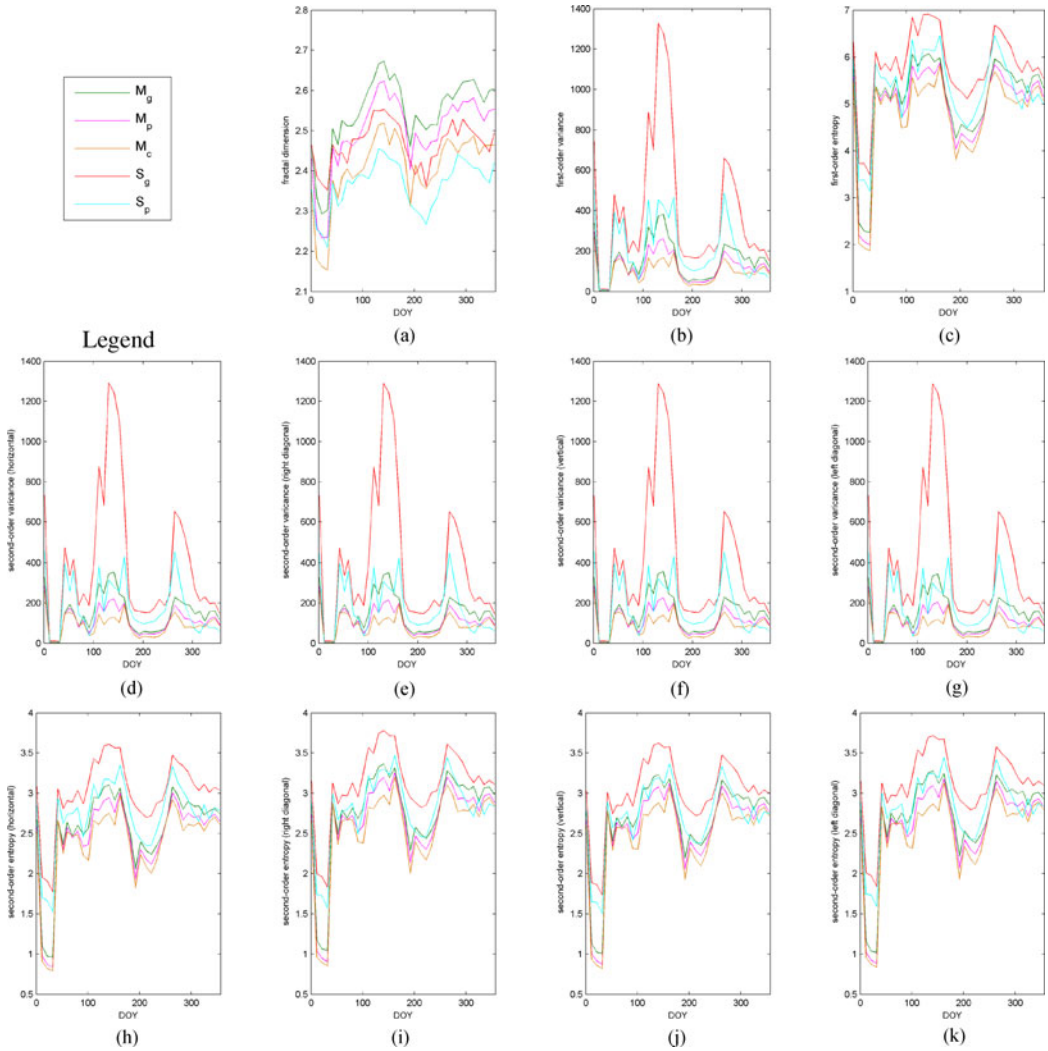

Fig. 6. Time series of features in the corn life cycle (taking the data from the state of Iowa for the year 2011 as an example). (a) Fractal dimension (FD); (b) first-order variance ($V_{1\text{st}}$); (c) first-order entropy ($E_{1\text{st}}$); (d) second-order variance (horizontal) ($V^{0}_{2\text{nd}}$); (e) second-order variance (right diagonal) ($V^{45}_{2\text{nd}}$); (f) second-order variance (vertical) ($V^{90}_{2\text{nd}}$); (g) second-order variance (left diagonal) ($V^{135}_{2\text{nd}}$); (h) second-order entropy (horizontal) ($E^{0}_{2\text{nd}}$); (i) second-order entropy (right diagonal) ($E^{45}_{2\text{nd}}$); (j) second-order entropy (vertical) ($E^{90}_{2\text{nd}}$); (k) second-order entropy (left diagonal) ($E^{135}_{2\text{nd}}$). The *x*-axis represents day of year (DOY), and the *y*-axis indicates the value of the corresponding feature. The reference tables between DOY and calendar dates can be found at (*http://disc.gsfc.nasa.gov/julian_calendar.shtml*).

In our results, time series of variance differ greatly, especially around the two peaks [as shown in Fig. 6(b) and (d)–(g)]. For instance, in Fig. 6(b), the curve of S_g dramatically deviates from the other curves. In contrast, the time series of fractal dimension [as shown in Fig. 6(a)] depict great similarity, i.e., the peaks are well aligned, which indicates superior consistency and robustness to image properties (e.g., spectral characteristics, spatial resolution, and the degree of pixel mixing).

B. Similarity of the Time Series of Features

In this study, we conducted a pairwise comparison among the time series from the cropland masked NDVI images using cosine similarity metric shown in (7). Given the five cropland masked NDVI images, the possible number of feature pairs is ten. Yet, comparisons of some pairs are redundant. For instance, the similarity of M_c and M_g can be derived from the pairs of M_c and M_p, and M_p and M_g. Therefore, comparisons of five pairs were conducted, which include M_c and M_p, M_p and M_g, S_p and S_g, M_p and S_p, and M_g and S_g. The quantitative measurements of similarity are illustrated in a polar coordinate system in Fig. 7. Because the texture of corn fields is mostly isotropic, only results of horizontal direction for the second-order variance and the second-order entropy are shown. The evaluation of cosine similarity covers the three states over the 10-year period from 2002 to 2012.

For the fractal dimension depicted in Fig. 7(e), the discrepancy pertaining to the similarity between M_g and S_g is distinct over the three states. High similarity is primarily in the results of Illinois, and low similarity is noted in the results of Iowa. The first- and second-order entropy trends are similar to the fractal dimension [see Fig. 7(b) and (d)]. In contrast, low similarity of the first- and second-order variance appears in Nebraska [see Fig. 7(a) and (c)]. The similarity between M_g and S_g is relatively unstable because: 1) both M_g and S_g show full pixel mixing, and the corresponding image differs in spatial

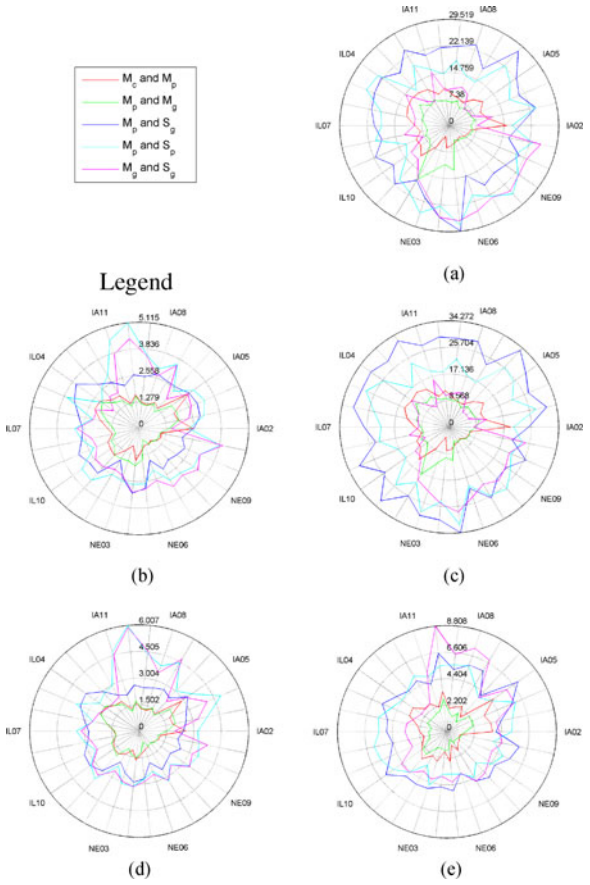

Fig. 7. Similarity of features from different cropland masked images. (a) First-order variance ($V_{1\mathrm{st}}$); (b) first-order entropy ($E_{1\mathrm{st}}$); (c) second-order variance (horizontal) ($V^0_{2\mathrm{nd}}$); (d) second-order entropy (horizontal) ($E^0_{2\mathrm{nd}}$); (e) fractal dimension (FD). Along the polar angle corresponds to a state in a given year, and the polar axis indicates the cosine similarity of a specific derived features. The measurement unit of the polar axis is degree (angle).

resolution (the effects of mixed pixels on each image are not the same and show uncertainty in the time series); and 2) they are derived from different sensors; thus, the spectral characteristics and spatial resolution inevitably affect the measurement of NDVI, and the effects on the pair are greater than those on other pairs.

As shown in Fig. 7(e), the highest similarity is observed for the pair M_p and M_g, followed by the pair M_c and M_p. However, the curves for the pairs M_p and M_g and M_c and M_p can be clearly distinguished as having been derived from the fractal dimension, but the curves for other features are not clear. This result was obtained because the fractal dimension, entropy, and variance were estimated by different spatial statistical methods. Entropy and variance indicate the statistical variation in the gray-level globally or within a certain directional space within a neighborhood. In this study, the fractal dimension considers the difference in gray level within a given neighborhood on different scales. In contrast to the first- and second-order entropy, the spectral characteristics of different imaging devises affect the fractal dimension to a lower extent than the spatial resolution and mixed pixels do. In general, the maximum of the similarity of the fractal dimension is 0.88, which is greater than that of the variance (either first- or second-order variance) and is comparable to that of the entropy (either first- or second-order entropy).

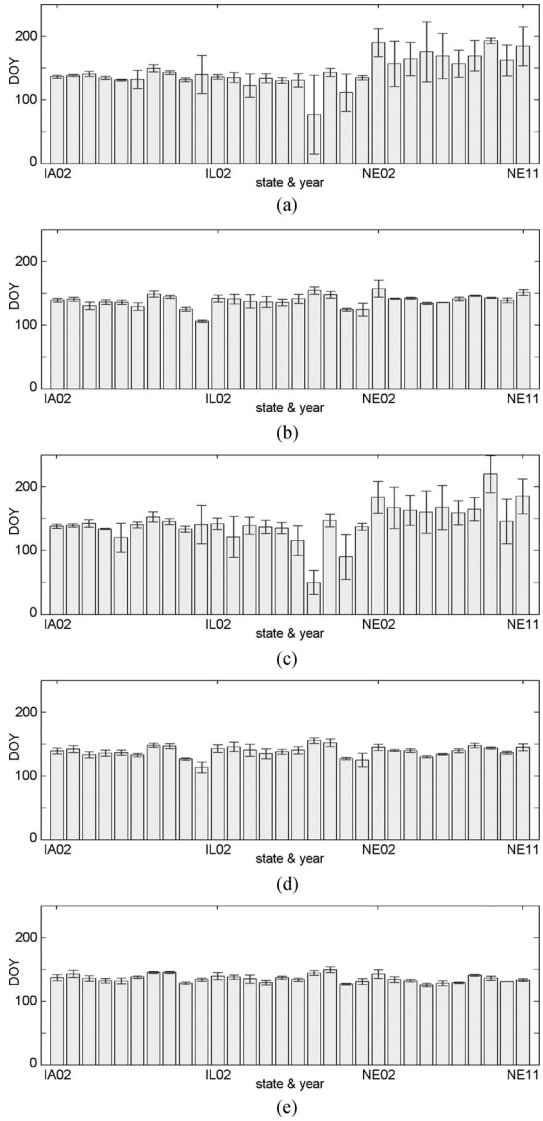

Fig. 8. Mean and standard deviation of the detected first peak from the features of different cropland masked images. The *x*-axis marks the state-year combination and the *y*-axis presents the day of year. The columns depict the average day of the detected emerged stage and the error bars show the corresponding standard deviation. (a) First-order variance ($\mathrm{V}_{1\mathrm{st}}$). (b) First-order entropy ($\mathrm{E}_{1\mathrm{st}}$). (c) Second-order variance (horizontal) ($V^0_{2\mathrm{nd}}$). (d) Second-order entropy (horizontal) ($E^0_{2\mathrm{nd}}$). (e) Fractal dimension.

C. Consistency of the Detected Phenology Stage

The first peak of fractal dimension time series corresponds to the emerged stage, a key phenology of corn crop. Successful detection of the first peak is an important indicator of the performance on characterizing corn phenology. Fig. 8 shows the accuracy of the first peak detection using the derived features. The *x*-axis is the state-year combination and the *y*-axis is the detected day of the start of the emerged stage. Each column depicts the average detected day. The error bar shows the standard deviation. Each state-year corresponds to five time series, and only if the first peak was detected, this feature derived from a

TABLE II
STABILITY OF THE FIRST-PEAK MEASURED BY THE NUMBER OF UNDETECTED PEAKS AND RMSE

	FD	V_{1st}	V^{0}_{2nd}	V^{45}_{2nd}	V^{90}_{2nd}	V^{135}_{2nd}
Undetected peaks	**10**	14	15	15	15	14
Relative RMSE*	**5.2**	20.2	20.6	22.3	20	25.8
Absolute RMSE	**8.1**	29.3	33.5	32.2	29.4	35.9
		E_{1st}	E^{0}_{2nd}	E^{45}_{2nd}	E^{90}_{2nd}	E^{135}_{2nd}
Undetected peaks		20	20	13	20	11
Relative RMSE*		5.6	5.4	5.6	5.4	6.4
Absolute RMSE		11.1	10.2	10.1	9.6	11.1

*The unit of RMSE error is day.

specific case of cropland masked images is taken into calculation of mean and standard deviation. For example, if the first peaks of S_g and S_p for the first-order entropy were undetectable in the year 2002 in Nebraska, then these two derived features are excluded in the mean and standard deviation calculation.

Among the five cases shown in Fig. 8, fractal dimension exhibits the smallest divergence, which implies the best consistency. The fractal dimension and entropy are better than the variance. Moreover, for the first-order variance, the earliest date of mean emerged stage appears on the 77th day of 2008 in Illinois, while the latest is the 193th day of 2009 in Nebraska. The difference between the earliest and latest corn emerged dates is up to 116 days, which is severely inconsistent to the actual agricultural production. Similarly, the high standard deviation appeared in the second-order variance.

Table II lists the number of the undetected peaks and the corresponding relative RMSE of each feature in all states and years. The undetected peaks appear to be concentrated in the dataset pertaining to the state of Nebraska. The undetected peaks of the fractal dimension occur in the time series derived from the SPOT-VGT sensor with corn-presence pixels (i.e., S_g). Non-crop covers such as natural forests are the inevitable factors that resulted in the misdetection. Although Nebraska ranks high in terms of cropland coverage in the Corn Belt, cropland pixels in Nebraska are greatly mixed with natural vegetation in contrast to that of Iowa and Illinois. As the degree of pixel-mixing increases, the corn phenology becomes more susceptible to the effects of other crops. The most serious case is the disappearing of bimodal distribution in the interannual time series. It is evident that the fractal dimension is the lowest for both the number of undetected peaks and the relative RMSE compared to other features.

Table II shows that the frequency of the missed peaks of the fractal dimension are concentrated in the time series derived from the SPOT-VGT sensor with the most mixed pixels (i.e., S_g). The spatial resolution of MODIS is 250 m, and that of SPOT-VGT is 1 km. According to measurements on Google Earth, the average size of a crop field is 1 km, which means that a MODIS pixel covers one-sixteenth of a crop field and SPOT-VGT covers only one field. The fractal dimension derived from M_g is more heterogeneous than that derived from S_g (see Fig. 7). In relative terms, the SPOT-VGT pixels are more susceptible to the interference of mixed pixels than the MODIS. S_g of

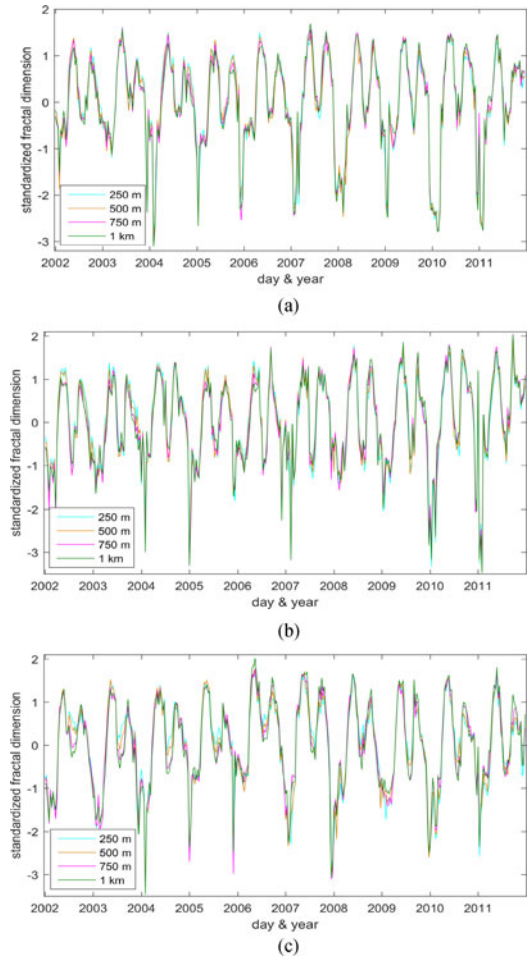

Fig. 9. Fractal dimension time series of corn-dominated MODIS 250-m data and its downsamped 500-m, 750-m and 1-km data. (a) State of Iowa. (b) State of Illinois. (c) State of Nebraska.

SPOT-VGT introduces more heterogeneous pixels than other combinations, e.g., M_g, M_p, M_c, and S_p. According to the Nyquist theorem, the sampling rate should be more than twice the highest-frequency component of the signal that is measured. Thus, the MODIS achieved better results than SPOT-VGT in crop analysis.

We also assessed the absolute RMSE of the first peak characterized by 11 diverse features. NASS's crop progress reports (CPRs) were regarded as the ground truth. The CPRs record the percent complete (area ratio) of crop fields that has either reached or completed a specific progress stage over a specific administrative unit. The dataset is distributed through NASS's "Quick Stats 2.0" service [46]. In this study, 50% completion of corn emerged progress indicates the emerged stage, and the piecewise cubic Hermite interpolating polynomial algorithm was employed to interpolate the crop progress observations [47]. The details of the data processing can be found in [11] and [48]. The absolute accuracy is presented Table II. It evident that the fractal dimension yielded the lowest absolute RMSE compared to that of the other features.

Our proposed algorithm eliminates the effect of irregular boundary shapes and provides a fractal dimension estimation

method for NDVI images. The error is primarily caused by overcounting or undercounting the number of boxes. Generally, undercounting occurred on a small scale, and overcounting occurred on a large scale if there is a uniform intensity area [49]. However, there are no true fractals in nature, i.e., in applying the mathematical theory of "exact" fractals to the "approximate" fractals of nature, errors are inevitable. Despite these limitations, the fractal dimension provides a critical and reliable measure for studying phenological patterns.

D. Sensitivity to Spatial Resolution

The spatial resolution is an important practical issue in real-world applications. To analyze the effect of the spatial resolution, we conducted experiments using MODIS images at four spatial resolutions. To simulate the coarse resolutions, we downsampled the MODIS with a pixel resolution at 250–500 -m, 750- m, and 1-km resolutions. The downsampling keeps every ith sample, where $i = 2, 3, 4$, to create a lower resolution image at 500 m, 750 m, and 1 km, respectively, in this study.

In our experiments, the degree of pixel mixing is 50%. Fig. 9 illustrates the time series of fractal dimension from 2002 to 2011 in the three states. Each plot consists of four curves that correspond to the aforementioned four spatial resolutions. The time series are normalized to have zero mean and unit standard deviation. It is clear that the curves are mostly overlapping for each state over a period of 10 years across three states despite the trivial amplitude difference at the peaks. It is evident that the time series of fractal dimension from images of various spatial resolution are very similar. This implies that the fractal dimension is mostly invariant to the change of image spatial resolution.

V. Conclusion

Fractal dimension-based methods for phenology analysis have demonstrated competitive effectiveness to per-pixel methods [35]. A major challenge faced by the computation of fractal dimension, however, is dealing with regions with irregular ROI. In this paper, we propose a method of estimating fractal dimension. Our method excludes volumes from noncubical space in the computation of fractal dimension and makes it independence from size and shape of the ROIs of interest. Hence, the computation of fractal dimension minimizes the bias from spatial irregularity that is common in real-world applications. Evaluation was conducted with NDVI products derived from MODIS and SPOT-VGT imagery from three states in the USA. These datasets present a tradeoff between spatial and temporal resolutions. Our method exhibited consistent performance with respect to spectral characteristics, spatial resolution, and degree of pixel mixing.

Our experimental results using the time series demonstrated that fractal dimension depicts great consistency and invariance to the change of image properties including spectral characteristics, spatial resolution, and the degree of pixel mixing. Fractal dimension considers the difference in gray level within a given neighborhood on different scales. In contrast to entropy, the spectral characteristics of different imaging devices exhibited lower impact to the fractal dimension, which implies its scale invariance. In general, the maximum of the similarity of the fractal dimension is 0.88, which is greater than that of the variance and is comparable to that of the entropy. With respect to the detection rate of the first peak, fractal dimension exhibits the smallest divergence, which implies the best consistency. It is evident that the fractal dimension yielded the lowest number of undetected peaks and the RMSE (relative and absolute) compared to other features. In summary, our proposed method for computing fractal dimension provides a reliable measure for studying phenology and improves the accuracy of crop phenology detection.

Our proposed fractal dimension estimation method is of interest to the communities of image processing and remote sensing, which provides a novel method for characterizing texture and can also be used in image segmentation, object tracking, etc. It presents a new dimension of feature for various ground objects. With our proposed method, the limitation of employing irregular ROI is mostly circumvented, which facilitates feature extraction with a greater degree of accuracy. The results are also beneficial to practitioners in agriculture and officials of land-use planning. In our future work, we plan to extend our proposed method and evaluate it in applications such as land cover classification.

References

[1] B. A. Bradley and J. F. Mustard, "Comparison of phenology trends by land cover class: A case study in the great basin," *USA. Glob. Change Biol.*, vol. 14, pp. 334–346, 2008.

[2] M. Fenner, "The phenology of growth and reproduction in plants," *Perspect. Plant Ecol.*, vol. 1, pp. 78–91, 1998.

[3] J. Pena-Barragan, M. Ngugi, R. Plant, and J. Six, "Object-based crop identification using multiple vegetation indices, textural features and crop phenology," *Remote Sens. Environ.*, vol. 115, pp. 1301–1316, 2011.

[4] M. Zhang, B. Wu, M. Yu, W. Zou, and Y. Zheng, "Crop condition assessment with adjusted NDVI using the uncropped arable land ratio," *Remote Sens.*, vol. 6, pp. 5774–5794, 2014.

[5] W. Scheftic, X. Zeng, P. Broxton, and M. Brunke, "Intercomparison of seven NDVI products over the United States and Mexico," *Remote Sens.*, vol. 6, pp. 1057–1084, 2014.

[6] J. Hatfield and J. Prueger, "Value of using different vegetative indices to quantify agricultural crop characteristics at different growth stages under varying management practices," *Remote Sens.*, vol. 2, pp. 562–578, 2010.

[7] É. L. Simms and H. Ward, "Multisensor NDVI-based monitoring of the Tundra-Taiga interface (mealy mountains, Labrador, Canada)," *Remote Sens.*, vol. 5, pp. 1066–1090, 2013.

[8] X. Zhang, M. A. Friedl, C. B. Schaaf, A. H. Strahler, J. C. F. Hodges, F. Gao, B. C. Reed, and A. Huete, "Monitoring vegetation phenology using MODIS," *Remote Sens. Environ.*, vol. 84, pp. 471–475, 2003.

[9] T. Sakamoto, M. Yokozawa, H. Toritani, M. Shebayama, N. Ishitsuka, and H. Ohno, "A crop phenology detection method using time-series MODIS data," *Remote Sens. Environ.*, vol. 96, pp. 366–374, 2005.

[10] B. B. Mandelbrot, *The Fractal Geometry of Nature*. New York, NY, USA: Freeman, 1982.

[11] Y. Shen, L. Di, G. Yu, and L. Wu, "Correlation between corn progress stages and fractal dimension from MODIS-NVDI time series," *IEEE Geosci. Remote Sens. Lett.*, vol. 10, no. 5, pp. 1065–1069, Sep. 2013.

[12] S. Myint, "Fractal approaches in texture analysis and classification of remotely sensed data: Comparisons with spatial autocorrelation techniques and simple descriptive statistics," *Int. J. Remote Sens.*, vol. 24, pp. 1925–1947, 2003.

[13] L. Wu, Q. Qin, X. Liu, H. Ren, J. Wang, X. Zheng, X. Ye, and Y. Sun, "Spatial up-scaling correction for leaf area index based on the fractal theory," *Remote Sens.*, vol. 8, p. 197, pp. 1–15, 2016.

[14] B. Liang and X. Tong, "An evaluation of fractal characteristics of urban landscape in Indianapolis, USA, using multi-sensor satellite images," *Int. J. Remote Sens.*, vol. 34, pp. 804–823, 2012.
[15] M. AL-Hamdan, J. Cruise, D. Rickman, and D. Quattrochi, "Effects of spatial and spectral resolutions on fractal dimensions in forested landscapes," *Remote Sens.*, vol. 2, pp. 611–640, 2010.
[16] R. Fensholt, K. Rasmussen, T. Nielsen, and C. Mbow, "Evaluation of earth observation based long term vegetation trends—Intercomparing NDVI time series trend analysis consistency of Sahel from AVHRR GIMMS, terra MODIS and spot VGT data," *Remote Sens. Environ.*, vol. 113, pp. 1886–1898, 2009.
[17] C. Emerson, N. Lam, and D. Quattrochi, "A comparison of local variance, fractal dimension, and Moran's I as aids to multispectral image classification," *Int. J. Remote Sens.*, vol. 26, pp. 1575–1588, 2005.
[18] J. Sun and J. Southworth, "Remote sensing-based fractal analysis and scale dependence associated with forest fragmentation in an Amazon trinational frontier," *Remote Sens.*, vol. 5, pp. 454–472, 2013.
[19] N.-N. Lam, H.-I. Qiu, D. Quattrochi, and C. Emerson, "An evaluation of fractal methods for characterizing image complexity. cartogr," *Cartogr. Geogr. Inf. Syst.*, vol. 29, pp. 25–35, 2002.
[20] R. Amri, M. Zribi, Z. Lili-Chabaane, B. Duchemin, C. Gruhier, and A. Chehbouni, "Analysis of vegetation behavior in a North African semi-arid region, using spot-vegetation NVDI data," *Remote Sens.*, vol. 3, pp. 2568–2590, 2011.
[21] R. Quevedo, L. G. Carlos, J. M. Aguilera, and L. Cadoche, "Description of food surfaces and microstructural changes using fractal image texture analysis," *J. Food Eng.*, vol. 53, pp. 361–371, 2002.
[22] O. S. Al-Kadi and D. Watson, "Texture analysis of aggressive and nonaggressive lung tumor CE CT images," *IEEE Trans. Biomed. Eng.*, vol. 55, no. 7, pp. 1822–1830, Jul. 2008.
[23] B. Klinkenberg, "A review of methods used to determine the fractal dimension of linear features," *Math. Geol.*, vol. 26, pp. 23–46, 1994.
[24] W. Han, Z. Yang, L. Di, A. Yagci, and S. Han, "Making cropland data layer data accessible and actionable in GIS education," *J. Geography*, vol. 113, pp. 129–138, 2014.
[25] C. Emerson, "Multi-scale fractal analysis of image texture and patterns," *Photogramm. Eng. Remote Sens.*, vol. 65, pp. 51–61, 1999.
[26] W. Sun, G. Xu, P. Gong, and S. Liang, "Fractal analysis of remotely sensed images: A review of methods and applications," *Int. J. Remote Sens.*, vol. 27, pp. 4963–4990, 2006.
[27] E. Oczeretko, M. Borowska, I. Szarmach, A. Kitlas, J. Szarmach, and A. Radwaski, "Fractal analysis of dental radiographic images in the irregular regions of interest," in *Information Technologies in Biomedicine*, vol. 69. Berlin, Germany: Springer, 2010, pp. 191–199.
[28] K. Falconer, *Fractal Geometry: Mathematical Foundations and Applications,* 2nd ed. New York, NY, USA: Wiley, 2003.
[29] N. Sarkar and B. Chaudhuri, "An efficient approach to estimate fractal dimension of textural images," *Pattern Recognit.*, vol. 25, pp. 1035–1041, 1992.
[30] L. Telesca, A. Lanorte, and R. Lasaponara, "Investigating dynamical trends in burned and unburned vegetation covers using SPOT-VGT NDVI data," *J. Geophys. Eng.*, vol. 4, pp. 128–138, 2007.
[31] R. Amri, M. Zribi, Z. Lili-Chabaane, B. Duchemin, and C. Gruhier, "Spot vegetation time series analysis for qualification of droughts over the Kairouan plain (central Tunisia)," in *Global Vegetation Monitoring and Modelling*, Avignon, Feb. 2014.
[32] C. Tucker *et al.*, "An extended AVHRR 8km NVDI dataset compatible with MODIS and spot vegetation NVDI data," *Int. J. Remote Sens.*, vol. 26, pp. 4485–4498, 2005.
[33] P. Toukiloglou, "Comparison of AVHRR, MODIS and vegetation for land cover mapping and drought monitoring at 1 km spatial resolution," Ph.D. dissertation, Cranfield University, Cranfield, U.K., 2007.
[34] C. Alonso, R. Benito, and A. Tarquis, "Comparison of fractal dimensions based on segmented NDVI fields obtained from different remote sensors," in *Proc. Geophys. Res. Abstr.*, vol. 14, 2012, pp. 1–2.
[35] L. Di, G. Yu, B. Zhang, M. Deng, and Z. Yang, "A national crop progress monitoring system based on NASA earth science results," in *Proc. Amer. Geophys. Union Fall Meet., Amer. Geophys. Union*, 2011, pp. 1–2.
[36] B. Holben, "Characteristics of maximum-value composite images from temporal AVHRR data," *Int. J. Remote Sens.*, vol. 7, pp. 1417–1434, 1986.
[37] M. Brown, J. Pinzon, K. Didan, J. Morisette, and C. Tucker, "Evaluation of the consistency of long-term NVDI time series derived from AVHRR, SPOT-vegetation, SeaWiFS, MODIS, and Landsat ETM+ sensors," *IEEE Trans. Geosci. Remote Sens.*, vol. 44, no. 7, pp. 1787–1793, Jul. 2006.
[38] B. Deronde *et al.*, "15 years of processing and dissemination of spot-vegetation products," *Int. J. Remote Sens.*, vol. 35, pp. 2402–2420, 2014.
[39] Y. Shen, L. Wu, L. Di, G. Yu, H. Tang, G. Yu and Y. Shao, "Hidden Markov models for real-time estimation of corn progress stages using MODIS and meteorological data," *Remote Sens.*, vol. 5, pp. 1734–1753, 2013.
[40] P. Tan, M. Steinbach, and V. Kumar, *Introduction to Data Mining*. Reading, MA, USA: Addison-Wesley, 2005.
[41] F. A. Kruse, A.B. Lefkoff, and J.W. Boardman, "The spectral image processing system (SIPS)—Interactive visualization and analysis of imaging spectrometer data," *Remote Sens. Environ.*, vol. 44, pp. 145–163, 1993.
[42] P. Jonsson and L. Eklundh, "Timesat—A program for analyzing time-series of satellite sensor data," *Comput. Geosci.*, vol. 30, pp. 833–845, 2004.
[43] P. Jonsson and L. Eklundh, "Seasonality extraction and noise removal by function fitting to time-series of satellite sensor data," *IEEE Trans. Geosci. Remote Sens.*, vol. 40, no. 8, pp. 1824–1832, 2002.
[44] P. Culbert, A. Pidgeon, V. St-Louis, D. Bash, and V. Rsdeloff, "The impact of phenological variation on texture measures of remotely sensed imagery," *IEEE J. Sel. Topics Appl. Earth Observ.*, vol. 2, no. 4, pp. 299–309, Dec. 2009.
[45] G. Srinivasan and G. Shobha, "Statistical texture analysis," *World Acad. Sci., Eng. Technol.*, vol. 36, pp. 1264–1269, 2008.
[46] Q. stats 2.0, Jan. 7, 2015. [Online]. Available: http://quickstats.nass.usda.gov/
[47] D. Kahaner, C. Moler, and S. Nash, *Numerical Methods and Software*. Upper Saddle River, NJ, USA: Prentice-Hall, 1988.
[48] W. Sacks and C. Kucharik, "Crop management and phenology trends in the US corn belt: Impacts on yields, evapotranspiration and energy balance," *Agr. Forest Meteorol.*, vol. 151, pp. 882–894, 2011.
[49] J. Mishra and S. Mishra, *L-System Fractals*. Amsterdam, Netherlands: Elsevier Science, 2007.

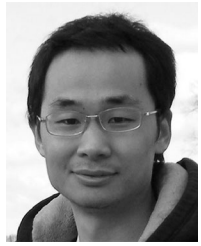

Yonglin Shen received the B.S. degree in geographic information system from the Wuhan University of Technology, Wuhan, China, in 2006, the M.S. degree in cartography and geography information system from Nanjing Normal University, Nanjing, China, in 2009, and the Ph.D. degree in cartography and geography information system from Beijing Normal University, Beijing, China, in 2013.

He is currently a Lecturer in the Collage of Information Engineering, China University of Geosciences, Wuhan. His research interests include remote-sensing-based phenology and drought monitoring.

Xiuguo Liu (M'16) received the B.E. and M.E. degrees in computer and application and the Ph.D. degree in cartography and geographic information engineering from the China University of Geosciences (CUG), Wuhan, China, in 1991, 1999, and 2004, respectively.

He is currently a Professor and an Associate Dean with the Faculty of Information Engineering, CUG. His research interests include polarimetric SAR theories, geographic information utilization, and 3-D geological modeling.

Xiaohui Yuan (S'01–M'05–SM'16) received the B.S. degree in electrical engineering from the Hefei University of Technology, Hefei, China, in 1996 and the Ph.D. degree in computer science from Tulane University, New Orleans, LA, USA, in 2004.

He is currently an Associate Professor with the University of North Texas, where he is also the Founder and Director of the Computer Vision and Intelligent Systems Laboratory. He is also a visiting Professor with the China University of Geosciences. His research interests include computer vision, data mining, machine learning, and artificial intelligence.